A Transient Pseudo-capacitor Using a Bioderived Ionic Liquid with Na Ions

*Shunsuke Yamada**

Shunsuke Yamada[1]

1 Department of Robotics, Division of Mechanical Engineering, Tohoku University, 6-6-01 Aoba, Aramakiaza, Aobaku, Sendaishi, Miyagi, 980-8579, Japan

*Corresponding author, e-mail: santa@tohoku.ac.jp

Keywords: Transient electronics, Pseudo-capacitor, Ionic gel, Electrolyte,

This is the peer reviewed version of the following article: https://onlinelibrary.wiley.com/doi/10.1002/smll.202205598, which has been published in final form at https://doi.org/10.1002/smll.202205598. This article may be used for non-commercial purposes in accordance with Wiley Terms and Conditions for Use of Self-Archived Versions. This article may not be enhanced, enriched or otherwise transformed into a derivative work, without express permission from Wiley or by statutory rights under applicable legislation. Copyright notices must not be removed, obscured or modified. The article must be linked to Wiley's version of record on Wiley Online Library and any embedding, framing or otherwise making available the article or pages thereof by third parties from platforms, services and websites other than Wiley Online Library must be prohibited.

Abstract

A pseudo-capacitor with transient behavior was applied in implantable, disposable, and bioresorbable devices, incorporating an Na ion-doped bioderived ionic liquid, molybdenum trioxide (MoO_3)-covered molybdenum foil, and silk sheet as the electrolyte, electrode, and separator, respectively. Sodium lactate is dissolved in choline lactate as a source of Na ions. The Experimental results reveal that the Na ions are intercalated into the van der Waals gaps in MoO_3, and the pseudo-capacitor shows an areal capacitance (1.5 mF/cm^2) that is three times larger than that without the Na ion. The fast ion diffusion of the electrolyte and the low resistance of the MoO_3 and Mo interface resulted in an equivalent series resistance of 96 Ω. A cycle test indicated that the pseudo-capacitor exhibited a high capacitance retention of 82.8% after 10 000 cycles. The transient behavior was confirmed by the dissolution of the pseudo-capacitor into phosphate-buffered saline solution after 101 days. Potential applications of transient pseudo-capacitors include electronics without the need for device retrieval after use, including smart agriculture, implantable, and wearable devices.

1. Introduction

Transient electronics[1], a new scheme of electronics that disappears after a prescribed time, offers emerging applications, including environmental sensing, implantable devices, and wearable devices for healthcare. Transient devices, transistors[2], sensors[3], and batteries[4] have been developed using biodegradable materials to reduce adverse effects on human bodies and the environment during decomposition. Supercapacitors (SCs) have high power density and cycle stability and are suitable for transient batteries. Lee et al. reported a transient SC using W, Fe, and Mo electrodes and NaCl solution as an electrolyte[5]. The W, Fe, and Mo metals exist in human bodies, show good biodegradability, and become oxides or hydroxides by hydrolysis to dissolve into the aqueous medium. Such biodegradability and dissolution kinetics are suitable for electrodes used in transient electronics. The SC with the Mo electrode exhibited an areal capacitance of 1.6 mF/cm^2 at a current density of 0.15 mA/cm^2. The SC was immersed in phosphate-buffered saline solution (PBS; 10×10^{-3} M, pH 7.4) at 37 ˚C, and the SC was fully dissolved in 9 days. In addition to the electrical double-layer capacitance, the adaption of faradaic or redox reactions is a promising charge storage method to boost the capacitance. Transition metal oxides possess a layered crystalline structure, which has a tiny gap called the van der Waals gap (vdW gap). Upon immersion of the metal oxides into electrolytes containing small ions, such as Li^+ and Na^+, the ions absorb and desorb onto the surface of the oxide, and the ions are intercalated and deintercalated into the vdW gap[6]. Such absorption and intercalation exhibit capacitive behavior, known as intercalation pseudo-capacitance[7]. Molybdenum trioxide (MoO_3) possesses a stacked nanosheet structure with the vdW gap of 0.69 nm[8], which enables accommodation of small ions to show the pseudo-capacitive behavior. Furthermore, MoO_3 shows biocompatibility and biodegradability[9] and researchers have reported biodegradable pseudo-capacitors (PC) using a MoO_3 layer as an electroactive material. Lee et al. reported a biodegradable SC, involving a serpentine-shaped Mo wire covered with an anodized Mo layer, a polyvinyl alcohol (PVA) gel containing a NaCl salt, and poly(1,8-

octanediol-co-citrate) (POC) as an electrode, electrolyte, and substrate, respectively[10]. The anodized Mo layers allow pseudo-capacitive behavior to increase the capacitance up to 4.2 mF/cm^2 at a current density of 0.05 mA/cm^2. A transience test reveals that the Mo wire, PVA electrolyte, and POC substrate dissolved into a deionized water (DIW). A bioresorbable SC was reported by Sheng et al., who used an amorphous molybdenum oxide (MoO_x) layer on a Mo foil[11]. A small flake structure on the MoO_x layer yields a large surface area which enables large electrical double layer capacitance, and furthermore, the intercalation pseudo-capacitance by Na ions increases capacitance to be 112.5 mF/cm^2 at 1.0 mA/cm^2. The SC decomposed after 40 days and 6 months in the in vitro and in vivo experiments, respectively. The aforementioned studies used aqueous electrolytes composed of salts and water that exist in human bodies. While electrolytes are biodegradable and bioresorbable and can be used for implantable and bioresorbable devices, aqueous electrolytes suffer from the evaporation of water and small potential windows of water.

As electrolytes for supercapacitors, ionic liquids are promising candidates owing to their large potential windows and low vapor pressure. Therefore, we developed a transient SC incorporating an ionic liquid (IL, (Tris(2-hydroxyethyl)methylammonium methylsulfate)), carbon, and Mo electrode, which decomposes upon contact with water[12]. Carbon can increase the accessible surface area of ions, which leads to a large electrical double-layer capacitance and low charge transfer resistance. The size of the ions in the IL is too large to show the pseudo capacitance associated with the intercalation of ions into the vdW gaps. Therefore, in previous works, metal ions, such as lithium (Li), have been doped into ILs, *N*-methyl-*N*-propyl-pyrrolidinium bis(trifluoromethanesulfonyl)imide ($[PYR_{13}][FSI]$)[13], 1-ethyl-3-methylimidazolium tetrafluoroborate ($[EMIM][BF_4]$)[14], or 1-Methyl-1-propylpyrrolidinium bis(trifluoromethylsulfonyl)imide (PMPyrrBTA)[15] for electrochemical devices. However, these ILs are toxic and have adverse effects on the human body and environment, which prevents the biodegradable and biocompatible application of IL[16].

Herein, we report a pseudo-capacitor that uses a bioderived IL, 2-Hydroxyethyl-trimethylammonium L-(+)-lactate ([Chol][Lac]) doped with Na ions and PVA to address this issue. The pseudo-capacitor (MoO_3-IGNa-PC) consists of a Mo electrode with a MoO_3 layer, silk separator, and electrolyte, as shown in **Fig. 1a**. A salt, sodium lactate ([Na][Lac]), dissolves into the IL (ILNa) as the Na ion source to obtain a triple ion system, [Chol][Na][Lac], and an ionic gel electrolyte (IGNa) made of IGNa and PVA shows an electrical double-layer capacitance and a pseudo capacitance attributed to the intercalation of Na^+ ions into the vdW gaps of the MoO_3 layers, as displayed in **Fig. 1b**. The Mo, MoO_3 electrode[5, 9-11, 17], PVA[18], choline[19], lactic acid[20], and silk fiber[21] (**Fig. 1c**) are biodegradable materials, and the SC (**Fig. 1d**) incorporates the materials showing good biodegradability. Scanning electron microscopy (SEM) observation of the intersection of the SC verifies that the silk separator and IGNa hold the parts rigidly and maintain the gap between the electrodes to avoid electrical shortages (**Fig. 1e**). Cyclic voltammetry (CV) revealed that MoO_3-IGNa-PC was electrochemically stable in the voltage range of 0 V to 1.2 V, which was approximately 50% larger than that of an SC with aqueous electrolytes. Galvanostatic charge-discharge (GCD) curves indicated that the MoO_3-IGNa-SC showed areal and volumetric capacitances of 1.5 mF/cm^2 and 0.74 F/cm^3, respectively, at a discharge current density of 0.2 mA/cm^2, and those values were 3 times as large as that without the Na ion. The MoO_3-IGNa-PC showed high capacitance retention of 82.8% after 10 000 cycles of charge and discharge at 0.2 mA/cm^2, and the equivalent series resistances (ESRs) were 96 Ω and 167 Ω after 1 and 10 000 cycles, respectively. The MoO_3-IGNa-PC was immersed in 10 mM PBS and gradually lost its mass and fully dissolved into the PBS after 101 days, leaving the silk separator and a small amount of the PVA and Mo electrode. The results show the pseudo-capacitive behavior of the triple ion system, [Chol][Na][Lac], and the transient behavior of–MoO_3-IGNa-PC. The biodegradable SC offers an opportunity to develop transient batteries that can be adapted in the fields of environmentally benign devices, sustainable electronics, and bioresorbable/implantable devices.

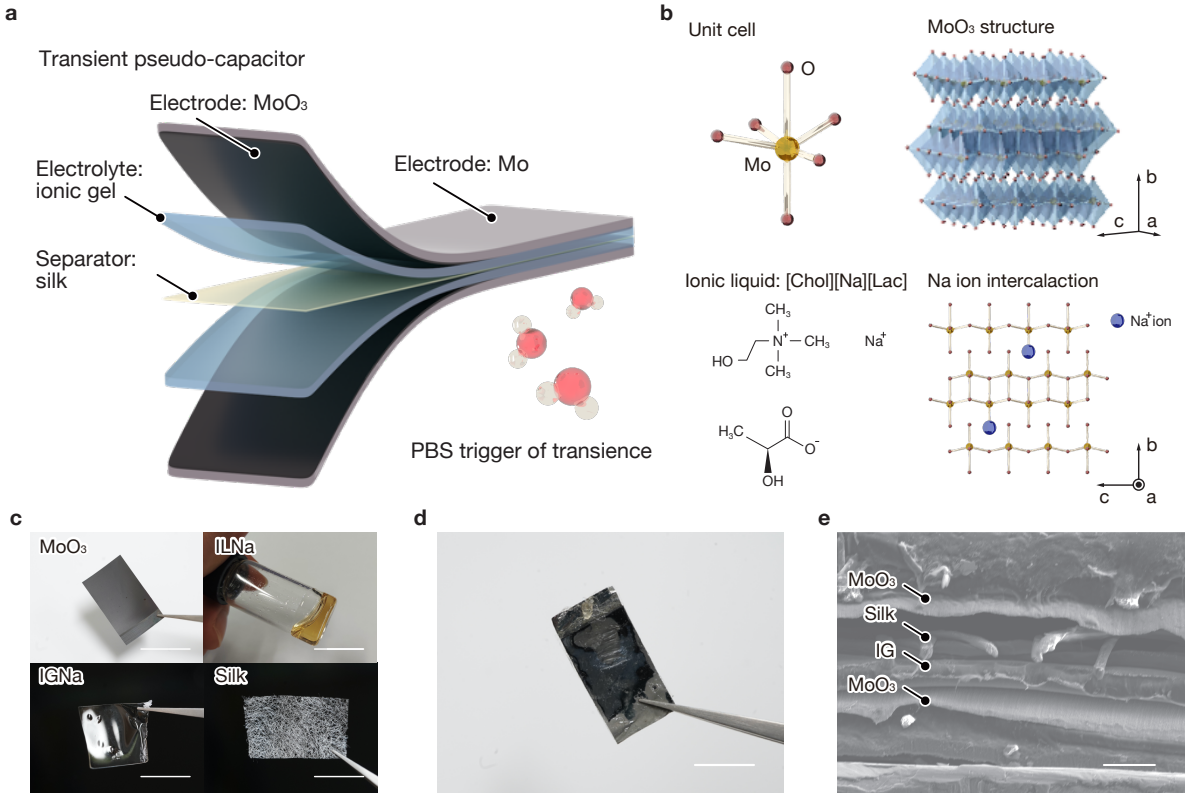

Fig. 1. Schematic illustration of (a) the transient pseudo-capacitor using the Mo electrode with the MoO_3 layer, ionic gel, and silk separator. (b) MoO_3 forms the stacked polyhedral structures consist of the multiple unit cells. The IL ([Chol][Na][Lac]) and MoO_3 electrode shows the pseudo-capacitive behavior by the intercalation of the Na ion into oxygen vacancy. (c) Photographs of the MoO_3 electrode, ionic liquid with the Na ions, ionic gel, and silk separator (Scale bar 10 mm). (d) A photograph (Scale bar 10 mm) and (e) SEM image of the intersection (Scale bar 80 μm).

2. Results and Discussion

2.1. Synthesis of the MoO_3 electrode

The fabrication of the MoO_3 electrode starts with the growth of a MoO_x layer on a Mo foil by an electrochemical reaction, based on previous studies[10-11]. A sheet of Mo foil was cut to dimensions of 35 mm × 35 mm (see **Fig. S1a**), and a silicone sheet with a square hole of 30 mm × 30 mm was placed on the Mo foil. The Mo foil and silicone sheet were held using a pair of PTFE plates, nuts, and bolts. The Mo foil was immersed in a 1M NaCl solution and anodized using a three-electrode cell with the Mo foil, Ag/AgCl electrode, and Pt electrode as the working, reference, and counter electrodes, respectively (**Fig. S2**). Linear sweep voltammetry (LSV) was performed on the Mo foil with a voltage range of 0 V to 0.8 V and scan speed of 0.1 V/s, for 80 cycles. The anodized Mo foil (MoO_x) exhibited a dark blue color (**Fig. S1b**), whereas the edge and the backside of the Mo foil maintained a silver color because the silicone sheet and PTFE jigs protected the areas from anodization. The anodized Mo was annealed in a glass furnace at 500 ˚C for 3 h in air to form a MoO_3 layer.

2.2. Characterization of the MoO_3 layer

As shown in **Fig. 2a**, observation of the surface of the MoO_3 layer by SEM reveals that the surface possesses flake structures with a size of up to 10 μm. The thickness of the MoO3 layer is of 1.5 μm as shown in **Fig. S3**. **Figure S4** shows the surface profiles of Mo, anodized Mo, and MoO_3 foils captured by a non-contact surface profiler (Zygo, Nexview NX2 3D Optical Profiler). The molybdenum, anodized Mo, and MoO_3 foils with dimensions of 167.595 μm × 167.595 μm possess surface area of 28088 μm^2, 28040 μm^2, and 27875 μm^2, respectively; the root mean square (RMS) roughness are of 0.15 μm, 0.16 μm, and 0.29 μm for the Mo, anodized Mo, and MoO_3 foils, respectively. The point scan of energy-dispersive X-ray spectroscopy (EDX) detected two sharp peaks attributed to Mo and oxygen (O) (**Fig. 2b**), where the peaks of C, Na, Pt, and Pd are ascribed to a carbon tape, Na absorbed into the MoO_3 layer during the

anodization, and Pt-Pd coating for the SEM observation, respectively. As shown in **Fig. 2c**, the corresponding maps of the Mo and O atoms captured by EDX in the image indicate that the O atom exists uniformly on the MoO_3 surface.

X-ray diffraction (XRD) analysis was performed on the foils of pristine Mo, MoO_x, and MoO_3 to determine the atomic structures. As shown in **Fig. 2d**, the XRD pattern of the pristine Mo foil shows sharp peaks at 40.4˚, 58.4˚, and 73.5˚, which is determined to be the (110), (200), and (211) crystal planes of Mo[22], respectively. For the MoO_x foil, peaks at 58.4˚ and 73.5˚ were detected in the XRD pattern and the Mo foil; meanwhile, the peak at 40.4˚ disappeared after anodization. The peaks at 58.4˚ and 73.5˚ could be ascribed to the pristine Mo foil underneath the MoO_x layer; hence, the anodized Mo layer could be in an amorphous state. The XRD pattern of MoO_3 showed peaks at 12.6˚, 22.9˚, 25.5˚, and 38.8˚ attributed to the (020), (110), (040), and (060) crystalline planes of MoO_3[7b, 22-23], respectively, in addition to the peaks at 58.4˚, and 73.5˚. The XRD pattern indicates that annealing allows the MoO_x amorphous structure to transform into the MoO_3 crystalline structure. Raman spectroscopy was performed on the foil of pristine Mo, anodized Mo, and MoO_3 for further analysis of the structural characteristics.

The pristine Mo and MoO_x foils did not exhibit distinguishable peaks in the narrow Raman spectra (**Fig. 2e**). Meanwhile, the MoO_3 foil showed peaks, which were attributed to the translational rigid chain (128 cm^{-1}), rotational rigid chain (157 cm^{-1}), O=Mo=O wagging (283 cm^{-1}), O-Mo-O bending (337 cm^{-1}), and stretching vibration modes for α-MoO_3 (666 cm^{-1})[11]. The two large peaks at 819 cm^{-1} and 995 cm^{-1} correspond to terminal Mo-O stretching and bridge Mo-O-Mo stretching, respectively, in polyhedrals distorted by oxygen vacancies[24].

X-ray photoelectron spectroscopy (XPS) was then performed to investigate the surface state of MoO_3. The survey spectrum of the MoO_3 foil is shown in **Fig. S5a**, and the Mo 3d and O 1S core level spectra are shown in **Fig. 2f**. The Mo 3d spectrum is deconvoluted, as shown in **Fig. S5b**, and intense peaks found at 232.9 eV and 236.0 eV ascribe to the Mo $3d_{5/2}$ and Mo $3d_{3/2}$ spin-orbit components, respectively, in the Mo^{6+} oxidation state[11, 25]. Minor peaks located

at 231.7 eV and 234.9 eV are attributed to the Mo $3d_{5/2}$ and Mo3 $d_{3/2}$, respectively, in the Mo^{5+} oxidation state; the presence of Mo^{5+} was calculated to be 3.7% based on the intensity of the Mo^{6+} and Mo^{5+} oxidation states. As shown in the deconvoluted O 1s spectrum in **Fig. S5c**, the sharp peak at 530.5 eV corresponds to the oxygen bond of Mo–O–Mo in molybdenum oxide, and the broad peak at 531.9 eV is attributed to oxygen species dissolved in the metal or adsorbed oxygen[11].

The survey, core level Mo 3d, and O 1s spectra of anodized Mo are shown in **Fig. S5d**, **e**, and **f**, respectively. Whereas intense peaks of Mo^{4+} and Mo^{5+} are found in the deconvoluted Mo 3d core level spectrum of anodized Mo, minor peaks of Mo^{5+} and no peaks of Mo^{4+} in the MoO_3 layer indicate that most of the reduced state of Mo oxidized to be Mo^{6+} oxidation state. According to the XRD, Raman, and XPS analyses, a crystalline MoO_3 layer was successfully synthesized on Mo foil.

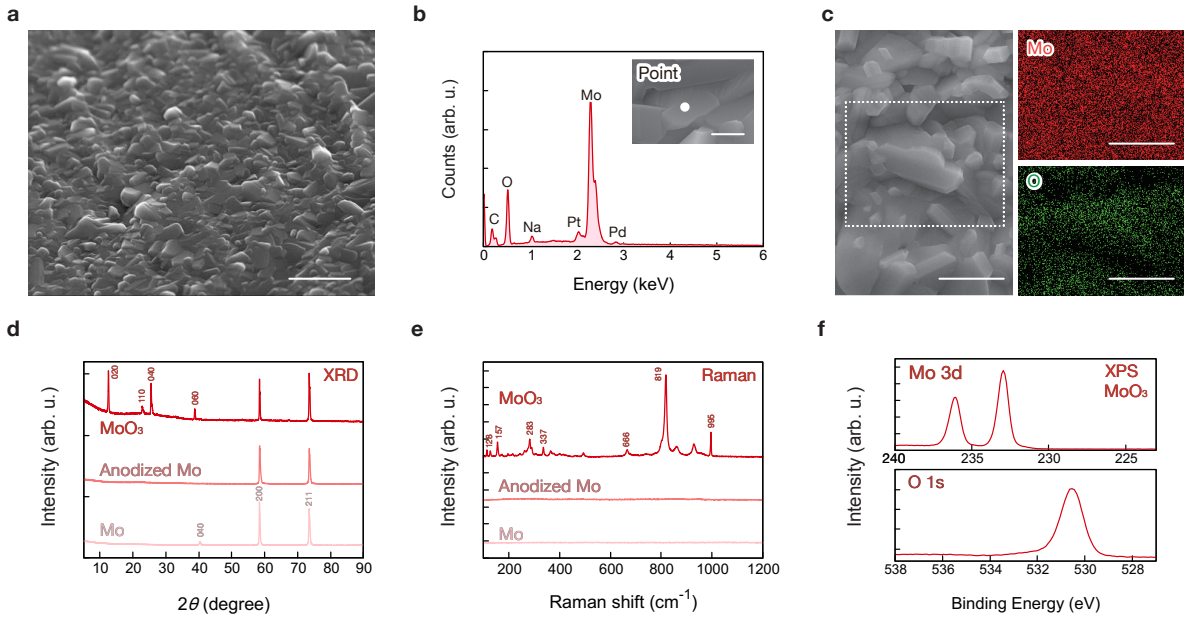

Fig. 2. Analysis on surface and crystalline structures of MoO_3. (a) A SEM image of the surface morphology of the MoO_3 electrode. (Scale bar 2 μm). (b) An EDX spectrum of the MoO_3 electrode. The inset shows the point of the scan (Scale bar 500 nm). (c) A SEM image and corresponding map of Mo and O, captured by EDX (Scale bar 2 μm). (d) XRD patterns and (e)

Raman spectra of Mo, anodized Mo, and MoO_3. (f) XPS spectra of Mo 3d and O 1s core levels of the MoO_3 electrode.

2.3. Preparation of ionic liquid with Na ions.

First, the residual moisture in the pristine ionic liquid (PIL) and salts was repelled via vacuum annealing at 80 ˚C for 24 h. The salt was dissolved in the IL using a magnetic stirrer, and the weight ratios of the salt were 5 wt%, 10 wt%, and 15 wt% with regard to the PIL. Unless otherwise noted, the IL containing Na ions of 5 wt%, 10 wt%, and 15 wt% are referred to as $ILNa_5$, $ILNa_{10}$, and $ILNa_{15}$, respectively.

2.4. Thermal Characteristics.

Fig. 3a shows the thermal profiles of PIL and ILNas obtained using differential scanning calorimetry measurements. The ILs were cooled to 143 K (-130 ˚C) and heated to 373 K (100 ˚C) at a scan rate of 10 K/min. The PIL shows a glass transition at 215.29 K (-57.86 ˚C), however, neither endothermic nor exothermic processes associated with crystallization of the ions were observed during the heating scan. The ILNas showed curves similar to those of the PIL. **Table S1** summarizes the glass transition temperatures. The temperature increased by more than 10 K with $ILNa_{15}$ compared with that of the PIL. The PIL and ILNas remained in the liquid state at temperatures ranging from -43 ˚C to 100 ˚C. This indicates that devices using ILs can operate in harsh environments[26].

2.5. Electrochemical measurement

Electrochemical impedance spectroscopy (EIS) was performed on the PIL and ILNas to investigate the influence of salt dissolution on ionic characteristics. **Fig. 3b** and **3c** show the schematic illustration and photograph of the experimental bed, respectively. **Fig. 3d** shows the

absolute impedance $|\boldsymbol{Z}|$ and phase $\boldsymbol{\theta}$ of the PIL and ILNas, respectively, with a frequency ranging from 10 mHz to 1 MHz using an EIS module (FRA32M, Autolab, Utrecht, Netherlands). With an increase in the weight ratios of the salts, $|\boldsymbol{Z}|$ in the high-frequency regime increases, and $\boldsymbol{\theta}$ in the high-frequency and low-frequency regimes decreases and increases, respectively. To investigate the influence of the weight ratio of metal ions on the ionic conductivity $\boldsymbol{\sigma}$, $\boldsymbol{\sigma}$ was calculated as:

$$\sigma = \frac{t}{AR}, \tag{1}$$

where $\boldsymbol{t}$, $\boldsymbol{A}$, and $\boldsymbol{R}$ are the gap between the electrodes, contact area between the IL and electrodes, and resistance at 100 kHz, respectively[27]. **Fig. 3e** shows $\boldsymbol{\sigma}$s of ILNas with respect to the weight ratio of the salts. The PIL exhibited a $\boldsymbol{\sigma}$ of 163 μS/cm, and the $\boldsymbol{\sigma}$s of $ILNa_{15}$ decreased with an increase in the weight ratio to 34 μS/cm. Previous studies revealed that a mixture of the IL, *N*-butyl-*N*-methylpyrrolidinium bis(trifluoromethanesulfonyl)imide ($[PYR_{14}][TFSI]$), and Na ion shows high viscosity and low ionic conductivity due to the enhancement of the interaction between the Na ion and [TFSI][28]. Such an interaction was also observed with a mixture of the IL, *N*-alkyl-*N*-methylpyrrolidinium bis(trifluoromethanesulfonyl)imide ($[PYR_{1R}][TFSI]$), and Li ion[13]. The interaction could occur between the metal ions and lactate in this work and reduce the ionic conductivity.

Fig. 3f shows the capacitance $\boldsymbol{C}$ of the PIL and ILNas at 1 Hz. $\boldsymbol{C}$ is given by the following equation[27, 29]:

$$C = \frac{1}{2\pi f|Z_{\mathrm{im}}|}, \tag{2}$$

where $\boldsymbol{f}$ and $\boldsymbol{Z}_{\mathrm{im}}$ are the frequency of the input signal and imaginary part of the impedance, respectively. Although $\boldsymbol{C}$s slightly decreased as the weight ratio of the salts increased, compared with the ionic conductivity, changes in $\boldsymbol{C}$s by doping with metal ions were not significant.

2.6. Potential window.

A study of the potential windows of the ILs was performed to investigate the influence of metal ions on electrochemical stability. A three-electrode cell with a glassy carbon electrode, Pt electrode, and Ag/Ag^+ electrode was used as the working, counter, and reference electrodes, respectively. **Fig. 3g, 3h,** and **3i** show the current-voltage curves of $ILNa_5$, $ILNa_{10}$, and $ILNa_{15}$, respectively, obtained using LSV at a scan rate of 5 mV/s. The current densities of the ILs are small because of the low ionic conductivity of the ILs, and, with such low current densities, the adaption of a certain cutoff current to determine the potential windows leads to unreasonably large potential windows. Therefore, we elucidated the potential window by the intersection of the lines in faradaic and non-faradaic regions obtained by a linear fitting method (see the LSV curves with fitting, **Fig. S6**), as previously reported[30]. **Table S2** summarizes the potential windows, cathodic limits, and anodic limits of the PIL and ILNa. The PIL and ILNas show potential windows of more than 3.0 V, which is more than three times larger than that of water. This large potential window enables a biodegradable SC with a high energy density. With an increase in the metal ions, the potential windows were slightly expanded by a few hundred millivolts; however, no current peak was detected within the potential windows. **Table 1** summarizes potential windows and ionic conductivities of ILs in recent literatures. Although the potential windows and ionic conductivities in this work are comparable with and a few magnitudes smaller than those in previous works, respectively, the biodegradability of the ILs in this work could be beneficial for the environment sensing and implantable devices.

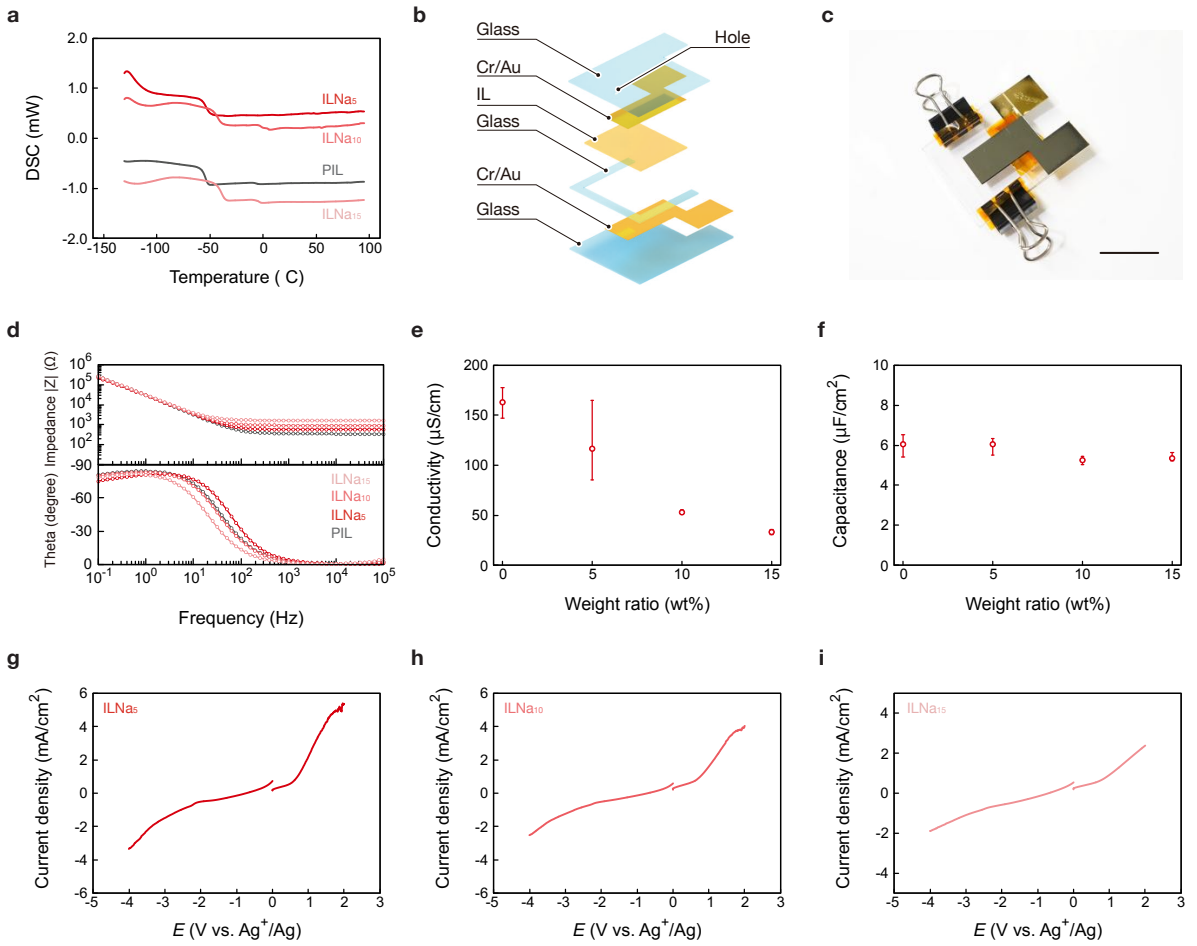

Fig. 3. (a) Differential scanning calorimetry profiles of the PIL and ILNas with a temperature range of -140 ˚C to 100 ˚C at a scan rate of 10 K/min. (b) Schematic and (c) photograph of the experimental setup (scale bar 20 mm). (d) Bode diagrams of the ILNas with a frequency range of 10 mHz to 1 MHz. Summary of (e) the ionic conductivities at 100 kHz and (f) capacitances at 1 Hz of the PIL and ILNas. Linear sweep voltammetry curves of the (g) $ILNa_5$, (h) $ILNa_{10}$, and (i) $ILNa_{15}$.

Table 1. Comparison of potential windows and ionic conductivities of ionic liquids.

No.	Ionic liquid	Potential window	Ionic conductivity	Year	Ref.
1	PIL	3.0 V	162 μS/cm^2	2022	This work
2	$ILNa_5$	3.4 V	116 μS/cm^2	2022	This work
3	$ILNa_{10}$	3.6 V	53 μS/cm^2	2022	This work
4	$ILNa_{15}$	3.5 V	51 μS/cm^2	2022	This work

5	[MTEOA][$MeOSO_3$]	-	228 μS/cm^2	2018	[4c]
6	[EtMeIm][BF_4]	4.595 V	14.4 mS/cm^2	2016	[30]
7	[EtMeIm][TFSI]	4.705 V	9.6 mS/cm^2	2016	[30]
8	[MePrIm][TFSI]	4.689 V	5.3 mS/cm^2	2016	[30]
9	[$BuNMe_3$][TFSI]	3.866 V	3.3 mS/cm^2	2016	[30]

2.7. Biodegradability of ionic liquid and gel.

A study on the biodegradability of the PIL and an ionic gel (IG) was performed according to OECD guidelines for testing of chemicals (OECD 301C modified MITI test (I))[31]. Most ILs are dispersed into gels to form IGs for various applications; therefore, IG composed of the 80 wt% PIL and 20 wt% PVA was subjected to a biodegradability test in addition to the PIL. Notably, the biodegradability of inorganic substances was not evaluated using the OECD 301C modified MITI test (I), and ILs with the Na ions were not investigated in the test. PIL and IG were added to basal culture media, and the solutions were incubated at 25 ˚C for 28 days, where a coulometer (OM3100A, Ohkura Electric Co., Ltd., Saitama, Japan) monitored the biological oxygen demand (BOD) in the samples. As shown in **Fig. S7a** and **S7b**, the BOD of the PIL and IG rapidly increases in four days and gradually increases as the day passes. Finally, the BOD of the PIL and IG reached 153 mg/l and 124 mg/l, respectively, and the PIL showed a higher BOD than that of the IG. Biodegradability (BD) is defined as the ratio of BOD with respect to the theoretical oxygen demand (ThOD) and is expressed by the following equation:

$$BD = \frac{BOD(\text{day}) - B(\text{day})}{ThOD} \times 100\ (\%), \qquad (3)$$

where BOD(day) and B(day) are the daily BOD and daily oxygen uptake in the blank inoculum control, respectively. The derivation of ThOD is discussed in the Supplementary Information. **Fig. S7c** and **S7d** show the biodegradability of the PIL ($BD_{\text{BOD\_PIL}}$) and IG ($BD_{\text{BOD\_IG}}$), respectively. The $BD_{\text{BOD\_PIL}}$ reached 70% in 6 days, whereas the maximum $BD_{\text{BOD\_IG}}$ was 54%

within 28 days. PVA is known as a biodegradable polymer[18c, 32], however, the biodegradation rate of PVA is moderate in the OECD test[33]. Therefore, PVA could slow the biodegradation rate of IG. The biodegradability of PIL and IG was also evaluated using dissolved organic carbon (DOC) before and after the test. The degradation of PIL (BD_{DOC_PIL}) and IG (BD_{DOC_IG}) is defined as:

$$BD_{DOC} = \frac{W_B - W_A}{W_B} \times 100\ (\%), \quad (4)$$

where W_A and W_B are the masses of residual carbon of the PIL or IG incubated with the basal culture medium and activated sludge and with water alone, respectively. As shown in **Table S3**, the biodegradation of PIL (BD_{DOC_PIL}) and IG (BD_{DOC_IG}) is 96.3% and 84.1%, respectively. The PIL exhibited a high degradation level, as confirmed by the BOD test. The degraded PIL in the IG was 76.8% (= 96.3% × 80%); hence, 7.3% of PVA could be decomposed by the activated sludge. The pass level of the OECD 301C modified MITI test (I) is 60% of ThOD and 70% removal of DOC[31], indicating that the PIL is biodegradable, and the IG does not involve ready biodegradability. Nonetheless, PVA is widely known as a biodegradable polymer, and a prolonged closed bottle test revealed 62% biodegradation of PVA (MW = 22 000) on day 108[33]. Therefore, IG is a promising material for transient electronics that disappears after use.

2.8. Electrochemical characterization of pseudo-capacitor.

Using $ILNa_{10}$ and MoO_3 electrode, the MoO_3-silk-MoO_3 was developed. The details of the fabrication of the pseudo-capacitor are summarized in the experimental section. Briefly, the IL and sodium-L-lactate were mixed using a magnetic stirrer to obtain a homogenous solution. The solution was dispersed in DIW with PVA and thoroughly mixed to form an IG precursor. A silk sheet and MoO_3 electrodes were laminated to form a MoO_3-silk-MoO_3 configuration using the IG precursor, followed by vacuum annealing at 80 ˚C to repel the moisture inside the pseudo-capacitor.

CV was performed on the pseudo-capacitors to investigate their electrochemical characterization. Unless otherwise noted, the experiments were performed in a chamber filled with 1-atm nitrogen gas. With scan rates varying from 5 mV/s to 1 V/s, the CV curves of the MoO_3-IGNa-PC maintain quasi-rectangular shapes up to 1 V/s, as shown in **Fig. 4a**. The developed MoO_3-IGNa-PC remained stable within the voltage range of 0 to 1.2 V while SCs with aqueous electrolytes showed a peak at 0.8 V due to a reaction between molybdenum trioxide and OH^- [11] written as

$$MoO_3 + 2OH^- \rightarrow HMoO_4^- + H_2O + e^-. \quad (5)$$

The electrode of molybdenum trioxide becomes a water-soluble specie, $HMoO_4^-$; the electrode gradually corroded by charge and discharge of supercapacitors.

To investigate the maximum applicable voltage on the MoO_3-IGNa-PC, the scan range was increased from 1.2 V to 1.5 V. As the upper limit of voltage increases, a current density evolves up to 0.3 mA/cm^2 with the voltage limit of 1.5 V, as shown in **Fig. S8**; hence, the maximum voltage (1.2 V) was applied in this study. To investigate the influence of the intercalation of Na ions into the MoO_3 layer, CV was performed on PCs with the MoO_3 electrode and IG (MoO_3-IG-PC) and with the Mo electrode and IGNa (Mo-IGNa-PC). The Mo-IGNa-PC showed a small current density compared to those of Mo-IG-PC and MoO_3-IGNa-PC (**Fig. 4b**). Although the XPS measurements revealed that the Mo foil was covered with native oxide (see XPS spectrum, **Fig. S5g**, **h**, and **i**), the oxide layer was considerably thinner than that of the MoO_3 electrode. Therefore, the electrical double-layer capacitance is more dominant than the pseudo-capacitance in the Mo-IGNa-PC, and the smooth Mo surface could result in a small surface area to show a small current density in the CV curve. For the MoO_3-IG-PC, the current density is higher than that of the Mo-IGNa-PC, because the MoO_3 foil involves microflakes on the surface to increase the surface area and boost the electrical double-layer capacitance. The CV curves of MoO_3-IGNa-PC show a rectangular shape with a larger area compared with that

of the MoO_3-IG-PC, and the Na ions in the IGNa could be intercalated into the vdW gaps in MoO_3 to form sodium MoO_x (Na_yMoO_x) as follows[11]:

$$\left(Mo^{2x}O_x\right)_{surface} + Na^+ + e^- \leftrightarrow \left(Mo^{2x-1}O_xNa\right)_{surface}, \quad (6)$$

$$MoO_x + ye^- + yNa^+ \leftrightarrow Na_yMoO_x. \quad (7)$$

As for the positive electrode anions absorbs on the surface of the MoO_3 electrode [34] written as

$$MoO_3 \leftrightarrow MoO_3 + //x[Lac]^- xe^- \ (//-\text{double layer}). \quad (8)$$

As displayed in **Fig. S9**, ex-situ XRD pattern shows significant change of the peaks before and after charging MoO_3-IGNa-PC at 1.2 V. The (020) and (060) peaks disappeared after charging. The change of the peaks results from loss of crystallinity of MoO_3 associated with the aforementioned crystal conversions. Such change of the ex-situ XRD pattern is observed in anodes for sodium ion batteries using transition metal oxide, MoO_3, $NiCo_2O_4$, and Sb_2O_4.[35] We assume that the MoO_3-IGNa-PC shows pseudo-capacitive behavior in addition to the electrical double-layer capacitance, which leads to a large current density.

GCD measurements were performed to investigate the capacitance of the MoO_3-IGNa-PC. As shown in **Fig. 4b**, a line in a GCD profile of the MoO_3-IGNa-PC at a charge and discharge current density of 0.20 mA/cm^2 is sloping and an almost symmetric triangular shape, which indicates that the developed MoO_3-IGNa-PC shows ideal capacitive behavior. Notably, the current density was calculated by dividing the applied current by the MoO_3 layer area. The areal capacitance, $\boldsymbol{C}_{areal}$, and volumetric capacitance, $\boldsymbol{C}_{vol}$, are defined as[34b, 36]

$$C_{\text{areal}} = \frac{i \times t}{S(V_{\text{e}} - V_{\text{d}})} \quad (9)$$

and

$$C_{\text{vol}} = \frac{i \times t}{TS(V_{\text{e}} - V_{\text{d}})}, \quad (10)$$

where $\boldsymbol{i}$ is the discharge current, $\boldsymbol{t}$ is the time of discharge, $\boldsymbol{T}$ is the thickness of the SC, $\boldsymbol{S}$ is the area of the MoO_3 layer, $\boldsymbol{V}_{\text{e}}$ is the voltage after charging, and $\boldsymbol{V}_{\text{d}}$ is the voltage drop during discharge. The $\boldsymbol{C}_{\text{areal}}$ and $\boldsymbol{C}_{\text{vol}}$ of the MoO_3-IGNa-PC at the discharge current density of 0.20 mA/cm^2 are 1.5 mF/cm^2 and 0.74 F/cm^3, respectively, as shown in **Fig. 4d** and **Fig. 4e**. The $\boldsymbol{C}_{\text{areal}}$ of the MoO_3-IGNa-PC at 0.20 mA/cm^2 is 2.8 times and 24 times larger than those of MoO_3-IG-PC and Mo-IGNa-PC, respectively, which indicates the enhancement of the capacitance by the pseudocapacitive behavior. With the increase in the discharge current density up to 2.0 mA/cm^2, the $\boldsymbol{C}_{\text{areal}}$ and $\boldsymbol{C}_{\text{vol}}$ of the MoO_3-IGNa-PC retain 0.76 mF/cm^2 and 0.38 F/cm^3, respectively. The MoO_3-IGNa-PC shows triangular shapes without a potential plateau in the GCD profile, and previous studies showed curves without a potential plateau, also using MoO_3 electrodes[37]. Previous studies have shown that a thick MoO_3 layer exhibits capacitive behavior that is similar to the electrical double-layer capacitive behavior in which SCs with carbon electrodes show[5]. The MoO_3-IGNa-PC shows a larger capacitance than that of the MoO_3-IG-PC in this study; thus, the MoO_3-IGNa-PC involves intercalation pseudo capacitance based on previous studies and this study.

Fig. 4f and **4g** show the areal and volumetric Ragone plots, respectively, where the areal energy density $\boldsymbol{E}_{\text{areal}}$, power density $\boldsymbol{P}_{\text{areal}}$, volumetric energy density $\boldsymbol{E}_{\text{vol}}$, and power density $\boldsymbol{P}_{\text{vol}}$ are defined by the following equations[34b, 36]:

$$E_{\text{areal}} = \frac{1}{2} \times C_{\text{areal}} \times \frac{(V_{\text{e}} - V_{\text{d}})^2}{3600}, \quad (11)$$

$$P_{\text{areal}} = \frac{E_{\text{areal}}}{t} \times 3600, \tag{12}$$

$$E_{\text{vol}} = \frac{1}{2} \times C_{\text{vol}} \times \frac{(V_{\text{e}} - V_{\text{d}})^2}{3600}, \tag{13}$$

$$P_{\text{vol}} = \frac{E_{\text{vol}}}{t} \times 3600. \tag{14}$$

As shown in **Fig. 4f**, the maximum $\boldsymbol{E}_{\text{areal}}$ is 0.12 μWh/cm^2 at the $\boldsymbol{P}_{\text{areal}}$ of 0.10 mW/cm^2, and the maximum $\boldsymbol{P}_{\text{areal}}$ is 0.59 mW/cm^2 at the $\boldsymbol{E}_{\text{areal}}$ of 20 nWh/cm^2. The values of the maximum $\boldsymbol{E}_{\text{areal}}$ and $\boldsymbol{P}_{\text{areal}}$ correspond to the $\boldsymbol{E}_{\text{vol}}$ of 40 μWh/cm^3 at the $\boldsymbol{P}_{\text{vol}}$ of 0.34 mW/cm^3 and $\boldsymbol{P}_{\text{vol}}$ 197 mW/cm^3 at the $\boldsymbol{E}_{\text{vol}}$ of 6.9 μWh/cm^3, respectively. The maximum $\boldsymbol{E}_{\text{areal}}$ and $\boldsymbol{P}_{\text{areal}}$ are comparable to those of transient SCs using Mo foil[5], serpentine anodized Mo wires[10], and carbon electrodes[38]. Although the maximum $\boldsymbol{E}_{\text{areal}}$ and $\boldsymbol{P}_{\text{areal}}$ are relatively low compared with commercial and previously reported SCs, the MoO_3-IGNa-PC possesses the capacity to enhance the capacitance by adapting nanomaterials with large surface areas, including nanowires of MoO_3[7b] and MXene[39].

A cycle test was performed on the MoO_3-IGNa-PC. **Fig. 4h** shows capacitance retention during charge and discharge cycles at 0.2 mA/cm^2, and the capacitance retention remains 82.8% after 10 000 cycles. **Fig. 4i** displays the Nyquist plots of the MoO_3-ILNa-PC with a frequency range of 10 mHz to 1 MHz after the first and last cycles. In the high-frequency regime, both plots show straight curves at 45° with respect to the real part of impedance ***Z'***, and the response could correspond to Na^+ ion intercalation into the vdW gap of the MoO_3 layer[40]. The intercalation of Na^+ was also observed in the CV profile as the current density increased owing to the doping of Na^+ ions into the IL. The ESRs were calculated by inserting approximated curves using the least squares method and finding intercepts between the lines and ***Z'***. As shown

in the inset, the ESR after the first cycle is 96 Ω, which is comparable to those of SCs with aqueous electrolytes and Mo or MoO_3 electrodes[5, 10-11]. Such a low ESR is attributed to the thin layer of the IG electrolyte by a silk fiber separator, low contact resistance between the Mo and MoO_3 interface, and/or fast diffusion of the Na^+ ions. The semicircle profile in the high-frequency region is negligibly small, and this behavior indicates a small charge-transfer resistance. The ESR increased to 167 Ω after the last cycle, and the MoO_3 electrode was degraded by the intercalation and deintercalation of Na^+ ions during the cycle test. The semicircle curve in the high-frequency regime is obvious after the last cycle, which implies an increase in the charge transfer resistance owing to the degradation of the electrode.

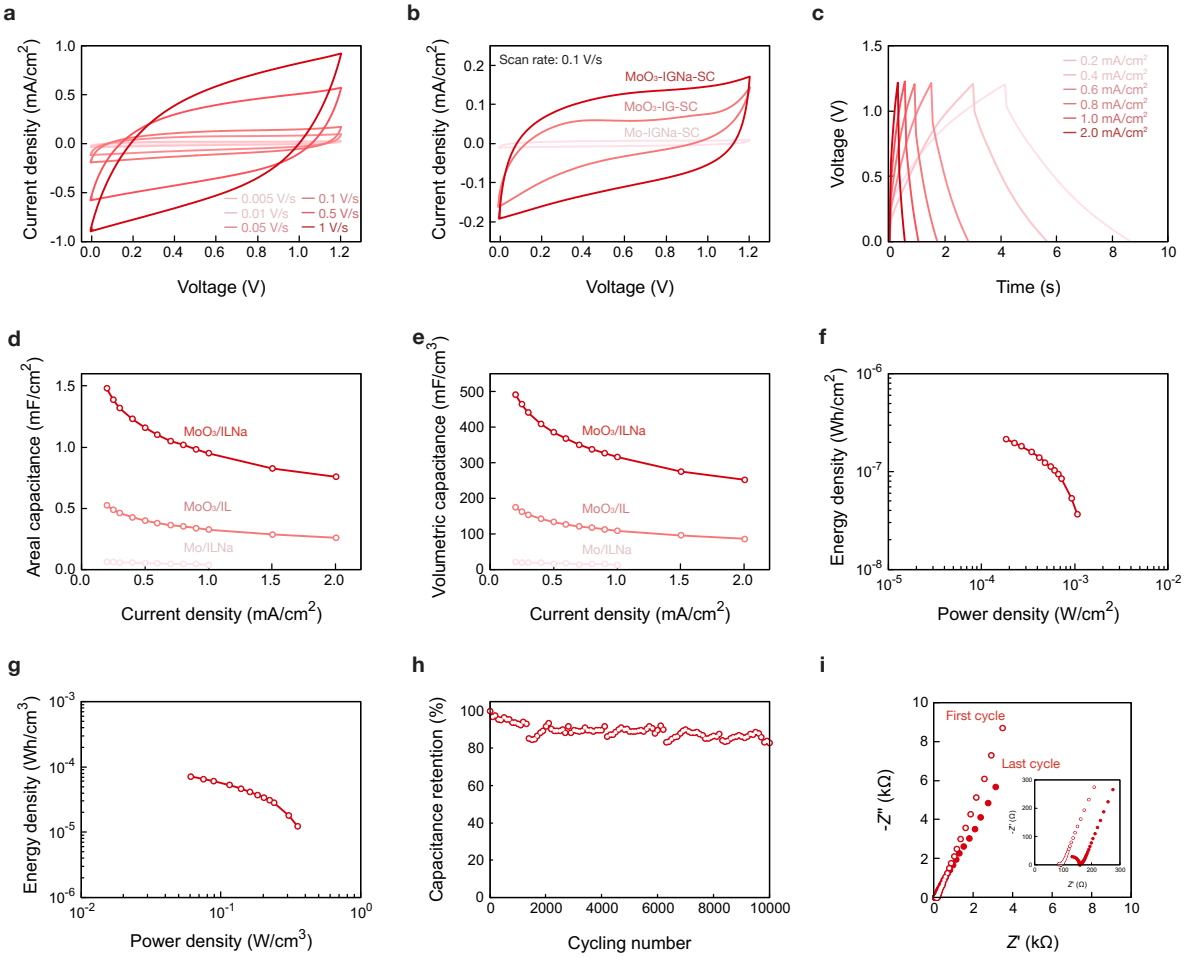

Fig. 4. Electrochemical characteristics on the pseudo-capacitor. (a) Cyclic voltammetry (CV) profiles of the MoO_3-IGNa-PC with scan rates of 5 mV/s to 300 mV/s. (b) Comparison of the CV curve of the MoO_3-IGNa-PC with the Mo-IGNa-PC and the MoO_3-IG-PC with a scan rate

of 0.1 V/s. (c) Galvanostatic charge-discharge (GCD) curves of the MoO_3-IGNa-PC with various current densities of 0.2 mA/cm^2 to 2.0 mA/cm^2. (d) The areal and (e) volumetric capacitances of the MoO_3-IGNa-PC, Mo-IGNa-PC, and MoO_3-IG-PC at different discharge currents. (f) The areal and (g) volumetric Ragone plots of the MoO_3-IGNa-PC. (h) The change in capacitance retention during a cycle test at a charge and discharge current of 0.2 mA/cm^2. (i) The Nyquist plots after the first and last cycles with frequencies of 10 mHz to 1 MHz. The inset is a magnified view of the plots.

Fig. 5a displays the CV curves of the MoO_3-IGNa-PCs of one and two cells in parallel with a scan rate of 50 mV/s. The current density of the two cells in parallel was approximately doubled compared to that of one cell and showed no peak in the CV profile. According to the GCD profiles shown in **Fig. 5b**, the charge and discharge times of the two cells in parallel are twice as large as those of one cell. The capacitances of one cell and two cells in parallel are defined as

$$C_{\text{areal}} = \frac{i \times t}{V_{\text{e}} - V_{\text{d}}}, \tag{15}$$

which are 1.5 mF and 3.1 mF at a discharge current of 0.2 mA, respectively. The capacitance with two cells in parallel remains approximately doubled with the current ranging from 0.2 mA to 2.0 mA compared with the capacitance of one cell, as shown in **Fig. 5c**.

The two cells of the MoO_3-IGNa-PCs in a series show no peak with a voltage ranging from 0 V to 2.4 V at a scan rate of 50 mV/s, as shown in **Fig. 5d**. The potential window is successfully expanded by a series connection of the MoO_3-IGNa-PCs, and the GCD profile was investigated in a voltage range of 0 V to 2.4 V. Although the voltage drop is obvious at the discharge, the line in the GCD profile is almost sloping, with a quasi-triangular shape with the discharge current density of 0.5 mA/cm^2. The capacitance of the MoO_3-IGNa-PCs in a series was 0.73 mF, which is almost half of that of one cell. **Fig. 5g** and **5h** show an electrical circuit

and a photograph of the MoO_3-IGNa-PCs in a series for LED illumination, respectively. The MoO_3-IGNa-PCs in a series were charged at 2.4 V and were able to illuminate a red LED for 5 s (**Fig. 5i**).

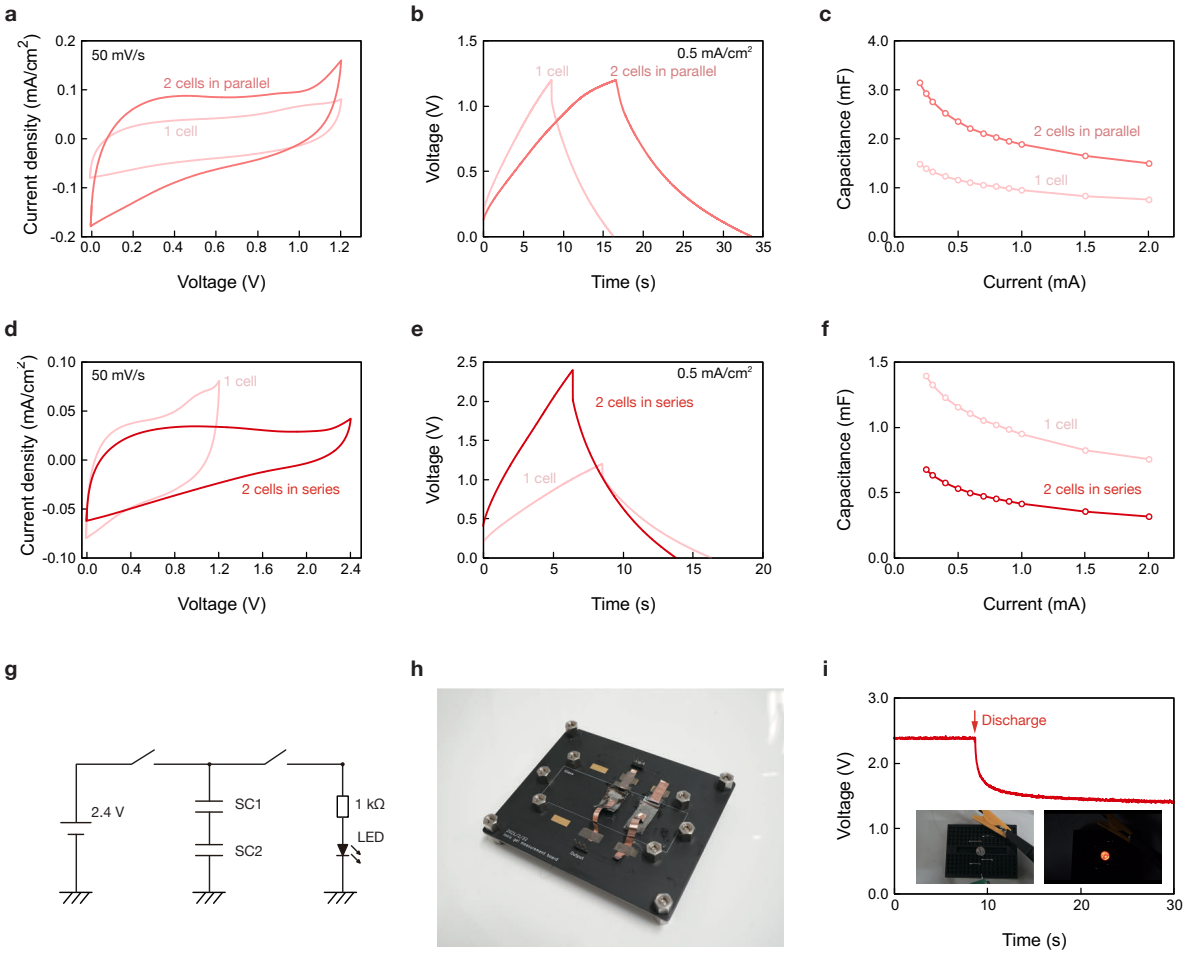

Fig. 5. Electrochemical characteristics on multiple MoO_3-IGNa-PCs connected in parallel and a series. (a) Cyclic voltammetry (CV) curves of one and two cells in parallel with a scan rate of 50 mV/s. (b) Galvanostatic charge-discharge (GCD) profiles of one and two cells in parallel with a current density of 0.5 mA/cm². (c) The capacitance of one and two cells in parallel with various current densities from 0.2 to 2.0 mA/cm². (d) CV profile of one and two cells in a series with a scan rate of 50 mV/s. (e) GCD curves of one and two cells in a series with a current density of 0.5 mA/cm². (f) The capacitance of one and two cells in a series with various current densities from 0.2 to 2.0 mA/cm². (g) The electrical circuit to illuminate a LED. (h) The

photograph of the two MoO_3-IGNa-PCs. (i) The transient behavior of voltage at the two MoO_3-IGNa-PCs connected in a series during discharge. Photographs show the LED and illumination.

2.9. Dissolution of the pseudo-capacitor in PBS.

The MoO_3-IGNa-PC was soaked in 100 mL of 10 mM PBS at 37 ˚C to investigate its transient behavior. **Fig. 6** shows the changes in the mass and time-lapse photographs of the MoO_3-IGNa-PC. The MoO_3-IGNa-PC showed glossy gray and blue colors associated with Mo and MoO_x, respectively, on the first day (day 1). The Mo electrodes became dark gray (day 11) and gradually degraded to break down into pieces, creating a hole in the center (days 58 and 79). Finally, the MoO_3-IGNa-PC dissolved in PBS (day 101), leaving the silk separator, and a small amount of PVA and Mo (day 122). The separator did not dissolve in PBS, however, the silk was able to be degraded in the human body by proteolytic enzymes[41]. Although the silk separator was adapted to increase the yield of the fabrication of the PCs in this study, without the silk separator, the MoO_3-IGNa-PC could be fully degradable. The electrolyte is composed of water-dissolvable materials, PVA, and IL; therefore, the mass was reduced by 48% on the first day due to the dissolution of the electrolyte. The Mo electrodes then began to dissolve by hydrolysis, and the mass reduced linearly until Mo disappeared, with a dissolution rate of 320 μg/day. Notably, the mass of Mo that disappears from the MoO_3-IGNa-PC in a single day (320 μg) is as large as that of Mo, which is ingested by humans daily (300 μg)[42]. The Institute of Medicine, Food and Nutrition Board sets the adequate intake of choline at 425 and 550 mg/day for women and men aged ≥ 19 years[43], respectively. Lactic acid is generally recognized as a safe material by the United States Food and Drug Administration (FDA)[44]. Given the above regulations and previous studies, the MoO_3-IGNa-PC could be used as a power source for implantable devices without adverse effects on the human body. Further, the electrochemical stability of MoO_3 were investigated in a 10mM PBS + 30mM H_2O_2 solution modeling a corrosive environment in a

human body, based on the proposed protocol [45]. **Figure S10a** shows front and back sides of MoO_3 which covered with polyimide tape to expose the MoO_3 area of 10 mm × 15 mm to 10 mM PBS for the EIS measurement. Before soaking into the 10 mM PBS + 30 mM H_2O_2 solution, a pair of the MoO_3 in the 10mM PBS shows low impedance with a frequency range from 0.1 Hz to 1 MHz and conductive and capacitive behaviors in high and low frequency regimes as shown in **Fig. S10b**. As shown in **Fig. S10c** and **S10d**, the MoO_3 degraded within 1 day, and one the foil tear into 2 pieces. Molybdenum easily dissolves into H_2O_2 solution [7b], and the MoO_3-IGNa-PC needs encapsulation to be maintained in a human body. We, therefore, adapted a biodegradable polymer, poly(octanediol citrate) (POC) [46]as encapsulation for the MoO_3-IGNa-PC and a performed stability test. A pair of POC film with a thickness of ~ 2 mm were laminated on the top and bottom of the MoO_3-IGNa-PC, using the prepolymer of the POC as a sealing agent. Annealing at 120˚C for 12 h produced encapsulation of the MoO_3-IGNa-PC. Please note that Au wires with a diameter of 100 μm and conductive epoxy yielded the electrical contacts because Mo is subject to dissolve into the 10 mM PBS + 30 mM H_2O_2 solution and not suitable for the electrical connection. Figure S11a shows the MoO_3-IGNa-PC before and after encapsulation; the POC films sealed the MoO_3-IGNa-PC without gaps and holes. The encapsulated MoO_3-IGNa-PC was soaked into a 10 mM PBS + 30 mM H_2O_2 solution at 37˚C. Change of the CV curves of the encapsulated MoO_3-IGNa-PC at 0.1 V/s is small during the stability test as shown in Fig S11b, which indicates that the POC encapsulation efficiently protects the MoO_3-IGNa-PC from corrosion by the 10 mM PBS + 30 mM H_2O_2 solution. Whereas the MoO_3 degraded within 1 day without encapsulation, the encapsulated MoO_3-IGNa-PC did not show damage and corrosion of the electrodes on day 7 as shown in Fig S11c and S11d. Boutry et al., reported that a derivative of the POC, poly(octamethylene maleate (anhydride) citrate) (POMaC), provided efficient protection of a strain and pressure sensor for 3.5 weeks under an in vivo test [1b, 47]. The degradation of POMaC surface was more dominant

than that of the bulk; the POMaC prevented the penetration of solution inside[1b]. The encapsulation of POC also could be a promising candidate for the encapsulation of the MoO_3-IGNa-PC.

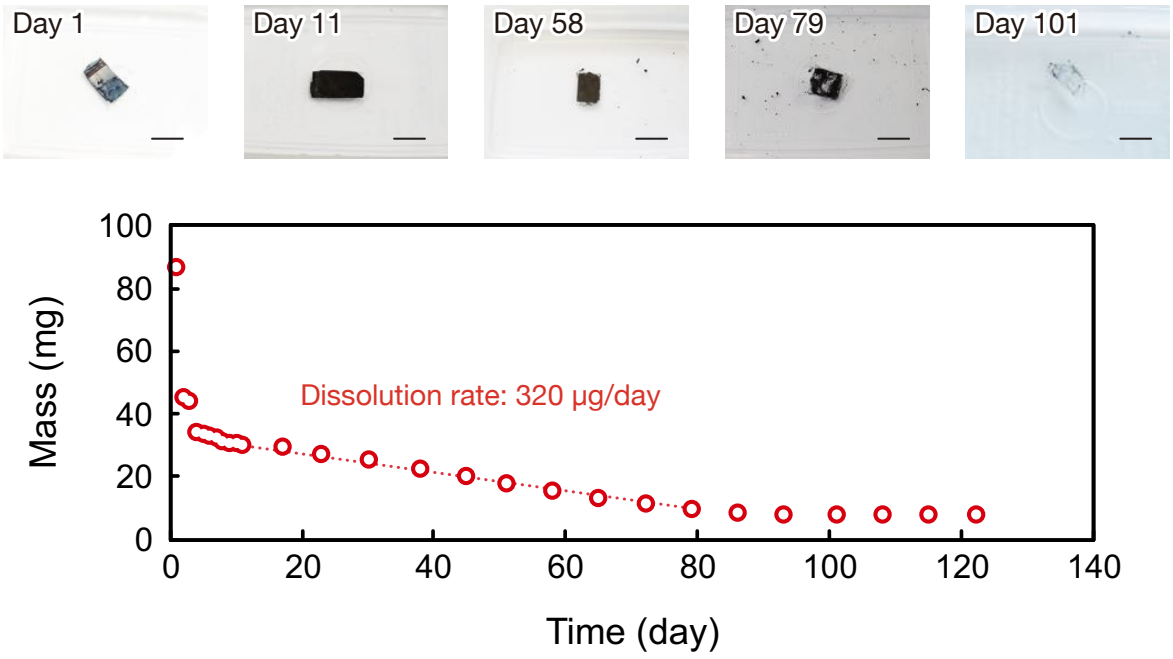

Fig. 6. Time-lapse photographs and the mass of biodegradable PC during the dissolution test. The Mo electrode showed a glossy gray color on day 1, and gradually shifted to dark gray associated with the oxidation (scale bar 10 mm). The PC finally dissolved, leaving the silk separator and small amount of PVA and the Mo electrode.

3. Conclusion

A transient pseudo-capacitor was successfully developed using biodegradable materials. A salt dissolved in an IL to form a triple ion system, and the Na ions in the IL showed repeatable intercalation and deintercalation into the vdW gaps in the MoO_3 layer grown on the Mo electrode. The intercalation pseudo-capacitive behavior resulted in high charge storage characteristics, low ESR, and cycle performance. The MoO_3-IGNa-PC was dissolved in PBS

for 101 days, leaving the silk separator and a small amount of PVA and the Mo electrode. The encapsulation with the POC provided efficient protection of MoO_3-IGNa-PC from the 10 mM PBS + 30 mM H_2O_2 solution which models body fluid. The transient pseudo-capacitor expands the opportunities for applications of the power source in biomedical, wearable, and environmentally benign devices.

Experimental Section

Fabrication of the MoO_x sheet. The fabrication was started by polishing a Mo foil (THE NILAC CORPORATION, MO-293171) with sandpaper, followed by cleaning with acetone, ethanol, and deionized water (DIW). The Mo foil was cut to 35 mm × 35 mm and the silicone sheet, which had a rectangular-shaped hole with a size of 30 mm × 30 mm, was placed on the Mo foil. The Mo foil and silicone sheet were held using a pair of PTFE covers with nuts and bolts. The Mo foil was immersed in a 1 M NaCl solution at 30 ˚C, and linear sweep voltammetry was performed on the Mo foil with a voltage range of 0 V to 0.8 V and a scan speed of 0.1 V/s, for 80 cycles using a three-electrode cell, the Mo foil, an Ag/AgCl electrode (RE-1B, ALS Co., Ltd, Tokyo, Japan), and Pt electrode (012961, ALS Co., Ltd) as a working electrode, reference electrode, and counter electrode, respectively. The anodized Mo was removed from the cover and annealed in a glass furnace at 500 ˚C for 3 h in air to obtain a MoO_3 sheet.

Preparation of the IL with metal ions: 2-hydroxyethyl-trimethylammonium L-(+)-lactate (product number: 670391, Sigma-Aldrich, MO, USA), lithium-L-lactate (product number: 120-03632, FUJIFILM Wako Pure Chemical Company, Osaka, Japan), sodium-L-lactate (product number: 71718-10G, Sigma Aldrich), and calcium lactate (product number: 533047, Fluorochem, Glossop, UK) were used according to the manufacturers' instructions. The IL and salts were kept in a vacuum oven for 24 h at 70 ˚C to repel residual moisture. Next, the salt was

added to the IL, where the weight ratios of the salts were 5 wt%, 10 wt%, and 15 wt% with regard to the IL; the mixtures were stirred vigorously until the salts dissolved. The homogenous solution was kept in an oven at 60 ˚C for 3 h to remove bubbles, followed by vacuum annealing for 24 h at 80 ˚C to repel residual moisture.

Electrochemical measurements for EIS: The electrodes were fabricated by cutting glass substrates and creating holes on the glass substrate to inject the ILs. The glass substrates were then cleaned with organic solvents, acetone, ethanol, and DIW, followed by cleaning with piranha solution containing 95% sulfuric acid (H_2SO_4) and 30% hydrogen peroxide (H_2O_2) in a volume ratio of H_2SO_4:H_2O_2 = 2:1. Chromium and gold with thicknesses of 20 and 200 nm, respectively, were deposited on the glass substrate by sputtering to fabricate electrodes using a stencil mask patterned with a laser cutter. Polyimide tape was laminated on the electrodes to create a contact area of 1 cm^2 between the ILs and electrodes. A pair of electrodes was assembled using a glass spacer with a thickness of 500 μm, followed by the injection of ILs through the holes. The EIS measurements were conducted using an EIS module (FRA32M, Autolab).

Electrochemical measurements for the potential window: Residual oxygen in the ILs was purged by bubbling N_2 gas for 30 min before LSV. The LSV for the potential window measurement was performed with a three-electrode cell, using glassy carbon (catalog ID: GC-3155, EC FRONTIER CO., LTD, Kyoto, Japan), Ag/Ag^+ (catalog ID: RE-12A, EC FRONTIER CO., LTD), and a Pt wire electrode (catalog ID: CE-300, EC FRONTIER CO., LTD) as the working, reference, and counter electrodes, respectively, where the reference electrode was filled with an acetonitrile electrolyte comprising 10 mM $AgNO_3$ and 100 mM NBu_4ClO_4. LSV was performed using a potentiostat (PGSTAT204, Autolab).

Biodegradation test: Biodegradability tests were performed according to the standard protocol of the OECD 301C modified MITI test (I). Before the test, the residual moisture in the PIL and IG was removed by vacuum annealing for 24 h at 80 ˚C. A basal culture medium (1 L) was prepared by mixing water and four 3 mL solutions named A, B, C, and D. The 100 mL solution A contained 2.18 g dipotassium hydrogenphosphate, 0.85 g potassium dihydrogenphosphate, 4.46 g disodium hydrogenphosphate 12-water, and 0.17 g ammonium chloride; the 100 mL solution B contained 2.25 g magnesium sulfate heptahydrate; the 100 mL solution C contained 2.75 g calcium chloride anhydrous; and the 100 mL solution D contained 0.025 g ferric chloride iron (III) chloride hexahydrate. BOD tests were performed on the samples (PIL and IG) with 300 mL basal culture medium, 9 mg activated sludge, and blank inoculum control, which consisted of 300 mL basal culture medium and 9 mg activated sludge. The samples were incubated for 28 days at 25±1 ˚C, where a coulometer (OM3100A, Ohkura Electric Co., Ltd.) monitored oxygen consumption and supplied oxygen in the same amount as that consumed. After incubation, the amount of residual carbon in the samples was analyzed using TOC measurement (multi N/C 3100, Analytik Jena, Jena, Germany).

Preparation of IG precursor: The salt, sodium-L-lactate (product number:71718-10G, Sigma-Aldrich) was dissolved in the IL, 2-hydroxyethyl-trimethylammonium L-(+)-lactate (product number: 670391, Sigma Aldrich), where the weight ratio of the salt was 10 wt% with regard to the IL. The DIW and PVA (molecular weight 89,000−98,000, 99^{+}% hydrolyzed, catalog ID 341584, Sigma-Aldrich) were added to the IL, where the weight ratio was DIW:PVA:IL = 8:1:4. The mixed solution was then heated at 110 ˚C for a few hours in an oven to obtain a homogenous solution of the IG precursor. An IL without Na ions was prepared in the same manner.

Fabrication of pseudo-capacitor: The MoO_3 foil was cut to make a 10 mm × 15 mm surface area of the MoO_3. The MoO_3 sheets were dip-coated with the IG precursor and dried for 24 h

at room temperature. A sheet of raw silk fiber was placed on one of the MoO_3 electrodes as a separator, and another MoO_3 electrode was laminated on the silk sheet using the IG precursor as glue, followed by drying at room temperature. The MoO_3-IGNa-PC was further dried in a vacuum oven at 80 ˚C. The Mo-IGNa-PC and MoO_3-IG-PC were fabricated in the same manner.

Synthesis of poly(octanediol citrate) (POC): Citric acid (251275-100G, Sigma-Aldrich) and 1,8-octanediol (EC No. 211-090-8, TOKTO CHEMICAL INDUSTRY CO., LTD.) with a molar ratio of 1:1 were added into a three-neck flask. The reactants were heated at 160˚C to melt with a magnetic stirrer under a N_2 stream, followed by further stirring at 140˚C for 40 min to produce a sticky and transparent precursor of the POC. Coating the inside of a glass container with 5 wt% poly(acrylic acid) (PAA) neutralized with sodium hydroxide to a pH of ~7.0 yielded a water-soluble sacrificial layer. The 10 g precursor of the POC was casted into the glass container and heated at 120 ˚C for 12 h to produce the ~2 mm thick POC film. The POC film was detached from the container, dissolving the sacrificial layer with DIW.

Encapsulation of pseudo-capacitor with POC: The MoO_3-IGNa-PC was packaged with POC films. A pair of the POC films were laminated on the top and bottom of the MoO_3-IGNa-PC with a POC precursor as a sealing agent, and the annealing in a vacuum oven at 100˚C for 12 h produced the encapsulated MoO_3-IGNa-PC, where gold wires with a diameter of 100 μm and conductive epoxy yielded the electrical contacts.

Characterization of MoO_3 sheet: The surface morphology and material composition of the MoO_3 electrode were observed using SEM (SU-70, Hitachi High-Technologies Corporation, Tokyo, Japan) and EDX (Aztec Energy X-max, Oxford Instruments, Abingdon, UK), respectively. A Bruker D8 ADVANCE instrument (Cu Kα; 0.15418 nm) was used for XRD measurements, where accelerating voltage and current are of 40 kV and 40 mA, respectively.

XPS and Raman spectra were obtained using a Raman spectrometer (NRS-5100, JASCO Corporation, Tokyo, Japan) and an XPS spectrometer (AXIS-ULTRA, Shimadzu Corporation, Kyoto, Japan), respectively.

Electrochemical measurements and LED illumination: The electrochemical measurements were conducted in a chamber filled with 1-atm of nitrogen. CV, GCD, and EIS measurements were conducted using a potentiostat and galvanostat (PGSTAT204, Autolab) with an EIS module (FRA32M, Autolab). A commercially available LED and a resistor of 1 kΩ were used for the LED illumination.

Dissolution of MoO_3-IGNa-PC and MoO_3 electrode: The 10 mM PBS solution was prepared by adding salts, NaCl (8.0 g), KCl (0.2 g), $Na_2HPO_4 \cdot 12H_2O$ (2.9 g), and KH_2PO_4 (2.9 g) into the DIW (1 L). Further, H_2O_2 were added into the PBS solution to model a corrosive environment in a human body. For the dissolution test, the MoO_3-IGNa-PC and a pair of MoO_3 foils were immersed in 100 mL of PBS and PBS + 30 mM H_2O_2, respectively, which were stored in an oven at 37 ˚C. The solutions were then refreshed daily.

Stability test on encapsulated MoO_3-IGNa-PC: The encapsulated MoO_3-IGNa-PC was soaked into 100 mL of PBS + 30 mM H_2O_2, which were stored in an oven at 37 ˚C. The solutions were then refreshed daily. The electrochemical characteristics were investigated after drying with a N_2 stream.

AUTHOR INFORMATION

Corresponding author
*E-mail: santa@tohoku.ac.jp
ORCID
Shunsuke Yamada: 0000-0002-9084-2070

NOTES

The authors declare no competing financial interest.

Acknowledgements
This work was supported in part by JSPS Grant-in-Aid for Early-Career Scientists 22K14213, and Toyota Physical and Chemical Research Institute.

Received: ((will be filled in by the editorial staff))
Revised: ((will be filled in by the editorial staff))
Published online: ((will be filled in by the editorial staff))

References

[1] a)S. W. Hwang, H. Tao, D. H. Kim, H. Y. Cheng, J. K. Song, E. Rill, M. A. Brenckle, B. Panilaitis, S. M. Won, Y. S. Kim, Y. M. Song, K. J. Yu, A. Ameen, R. Li, Y. W. Su, M. M. Yang, D. L. Kaplan, M. R. Zakin, M. J. Slepian, Y. G. Huang, F. G. Omenetto, J. A. Rogers, *Science* **2012**, 337, 1640; b)C. M. Boutry, Y. Kaizawa, B. C. Schroeder, A. Chortos, A. Legrand, Z. Wang, J. Chang, P. Fox, Z. Bao, *Nature Electronics* **2018**, 1, 314.
[2] a)F. Xia, T. Xia, L. Xiang, F. Liu, W. Jia, X. Liang, Y. Hu, *ACS Appl Mater Interfaces* **2022**; b)S. H. Jin, S. K. Kang, I. T. Cho, S. Y. Han, H. U. Chung, D. J. Lee, J. Shin, G. W. Baek, T. I. Kim, J. H. Lee, J. A. Rogers, *ACS Appl Mater Interfaces* **2015**, 7, 8268.
[3] a)Q. Yang, T. Wei, R. T. Yin, M. Wu, Y. Xu, J. Koo, Y. S. Choi, Z. Xie, S. W. Chen, I. Kandela, S. Yao, Y. Deng, R. Avila, T. L. Liu, W. Bai, Y. Yang, M. Han, Q. Zhang, C. R. Haney, K. Benjamin Lee, K. Aras, T. Wang, M. H. Seo, H. Luan, S. M. Lee, A. Brikha, N. Ghoreishi-Haack, L. Tran, I. Stepien, F. Aird, E. A. Waters, X. Yu, A. Banks, G. D. Trachiotis, J. M. Torkelson, Y. Huang, Y. Kozorovitskiy, I. R. Efimov, J. A. Rogers, *Nat Mater* **2021**, 20, 1559; b)G. A. Salvatore, J. Sülzle, F. Dalla Valle, G. Cantarella, F. Robotti, P. Jokic, S. Knobelspies, A. Daus, L. Büthe, L. Petti, N. Kirchgessner, R. Hopf, M. Magno, G. Tröster, *Advanced Functional Materials* **2017**, 27; c)M. Baumgartner, F. Hartmann, M. Drack, D. Preninger, D. Wirthl, R. Gerstmayr, L. Lehner, G. Mao, R. Pruckner, S. Demchyshyn, L. Reiter, M. Strobel, T. Stockinger, D. Schiller, S. Kimeswenger, F. Greibich, G. Buchberger, E. Bradt, S. Hild, S. Bauer, M. Kaltenbrunner, *Nat Mater* **2020**, 19, 1102; d)S. Yamada, H. Toshiyoshi, *ACS Appl Mater Interfaces* **2020**, 12, 36449; e)S. Yamada, T. Sato, H. Toshiyoshi, *Applied Physics Letters* **2017**, 110.
[4] a)W. Tian, Y. Li, J. Zhou, T. Wang, R. Zhang, J. Cao, M. Luo, N. Li, N. Zhang, H. Gong, J. Zhang, L. Xie, B. Kong, *ACS Appl Mater Interfaces* **2021**, 13, 8285; b)K. K. Fu, Z. Wang, C. Yan, Z. Liu, Y. Yao, J. Dai, E. Hitz, Y. Wang, W. Luo, Y. Chen, M. Kim, L. Hu, *Advanced Energy Materials* **2016**, 6; c)S. Yamada, H. Toshiyoshi, *Small* **2018**, 14, e1800937.
[5] G. Lee, S.-K. Kang, S. M. Won, P. Gutruf, Y. R. Jeong, J. Koo, S.-S. Lee, J. A. Rogers, J. S. Ha, *Advanced Energy Materials* **2017**, 7.
[6] T. Brezesinski, J. Wang, S. H. Tolbert, B. Dunn, *Nat Mater* **2010**, 9, 146.
[7] a)S. Maroufi, R. K. Nekouei, S. S. Mofarah, A. P. O'Mullane, Y. Yao, S. Lim, C. Cazorla, V. Sahajwalla, *Advanced Functional Materials* **2021**, 31; b)B. Yao, L. Huang, J. Zhang, X. Gao, J. Wu, Y. Cheng, X. Xiao, B. Wang, Y. Li, J. Zhou, *Adv Mater* **2016**, 28, 6353; c)W. Zheng, J. Halim, A. S. Etman, A. E. Ghazaly, J. Rosen, M. W. Barsoum, *Electrochimica Acta* **2021**, 370; d)B. T. Liu, X. M. Shi, X. Y. Lang, L. Gu, Z. Wen, M. Zhao, Q. Jiang, *Nat Commun* **2018**, 9, 1375.
[8] T. Tsumura, M. Inagaki, *Solid State Ionics* **1997**, 104, 183.
[9] a)Y. Liu, Y. Zheng, X. H. Chen, J. A. Yang, H. Pan, D. Chen, L. Wang, J. Zhang, D. Zhu, S. Wu, K. W. K. Yeung, R. C. Zeng, Y. Han, S. Guan, *Advanced Functional Materials*

2019, 29; b)L. Yin, H. Cheng, S. Mao, R. Haasch, Y. Liu, X. Xie, S. W. Hwang, H. Jain, S. K. Kang, Y. Su, R. Li, Y. Huang, J. A. Rogers, *Advanced Functional Materials* **2013**, 24, 645.
[10] H. Lee, G. Lee, J. Yun, K. Keum, S. Y. Hong, C. Song, J. W. Kim, J. H. Lee, S. Y. Oh, D. S. Kim, M. S. Kim, J. S. Ha, *Chemical Engineering Journal* **2019**, 366, 62.
[11] H. Sheng, J. Zhou, B. Li, Y. He, X. Zhang, J. Liang, J. Zhou, Q. Su, E. Xie, W. Lan, K. Wang, C. Yu, *Sci Adv* **2021**, 7.
[12] S. Yamada, *Acs Appl Mater Inter* **2022**, 14, 26595.
[13] W. A. Henderson, S. Passerini, *Chem Mater* **2004**, 16, 2881.
[14] K. Hayamizu, Y. Aihara, H. Nakagawa, T. Nukuda, W. S. Price, *Journal of Physical Chemistry B* **2004**, 108, 19527.
[15] D. P. Dubal, D. Aradilla, G. Bidan, P. Gentile, T. J. Schubert, J. Wimberg, S. Sadki, P. Gomez-Romero, *Sci Rep* **2015**, 5, 9771.
[16] T. P. Pham, C. W. Cho, Y. S. Yun, *Water Res* **2010**, 44, 352.
[17] L. Yin, X. Huang, H. Xu, Y. Zhang, J. Lam, J. Cheng, J. A. Rogers, *Adv Mater* **2014**, 26, 3879.
[18] a)H. Marušincová, L. Husárová, J. Růžička, M. Ingr, V. Navrátil, L. Buňková, M. Koutny, *International Biodeterioration & Biodegradation* **2013**, 84, 21; b)M. C. Lin, C. W. Lou, J. Y. Lin, T. A. Lin, Y. S. Chen, J. H. Lin, *Mater Sci Eng C Mater Biol Appl* **2018**, 91, 404; c)E. Chiellini, A. Corti, S. D'Antone, R. Solaro, *Progress in Polymer Science* **2003**, 28, 963.
[19] a)M. E. Vahter, *J Nutr* **2007**, 137, 2798; b)W. H. W. Tang, D. Y. Li, S. L. Hazen, *Nat Rev Cardiol* **2019**, 16, 137.
[20] a)S. Hui, J. M. Ghergurovich, R. J. Morscher, C. Jang, X. Teng, W. Lu, L. A. Esparza, T. Reya, Z. Le, J. Yanxiang Guo, E. White, J. D. Rabinowitz, *Nature* **2017**, 551, 115; b)B. Faubert, K. Y. Li, L. Cai, C. T. Hensley, J. Kim, L. G. Zacharias, C. Yang, Q. N. Do, S. Doucette, D. Burguete, H. Li, G. Huet, Q. Yuan, T. Wigal, Y. Butt, M. Ni, J. Torrealba, D. Oliver, R. E. Lenkinski, C. R. Malloy, J. W. Wachsmann, J. D. Young, K. Kernstine, R. J. DeBerardinis, *Cell* **2017**, 171, 358.
[21] a)Z. Wang, Y. Zhang, J. Zhang, L. Huang, J. Liu, Y. Li, G. Zhang, S. C. Kundu, L. Wang, *Sci Rep* **2014**, 4, 7064; b)H. Wang, F. Meng, Y. Cai, L. Zheng, Y. Li, Y. Liu, Y. Jiang, X. Wang, X. Chen, *Adv Mater* **2013**, 25, 5498; c)C. Hou, Z. Xu, W. Qiu, R. Wu, Y. Wang, Q. Xu, X. Y. Liu, W. Guo, *Small* **2019**, 15, e1805084; d)W. Y. He, C. Y. Wang, H. M. Wang, M. Q. Jian, W. D. Lu, X. P. Liang, X. Zhang, F. C. Yang, Y. Y. Zhang, *Sci Adv* **2019**, 5.
[22] J. S. Kang, J. Kim, M. J. Lee, Y. J. Son, D. Y. Chung, S. Park, J. Jeong, J. M. Yoo, H. Shin, H. Choe, H. S. Park, Y. E. Sung, *Adv Sci (Weinh)* **2018**, 5, 1700601.
[23] J. Zhou, S. Z. Deng, N. S. Xu, J. Chen, J. C. She, *Applied Physics Letters* **2003**, 83, 2653.
[24] a)G. Mestl, P. Ruiz, B. Delmon, H. Knozinger, *The Journal of Physical Chemistry* **1994**, 98, 11269; b)M. Dieterle, G. Weinberg, G. Mestl, *Physical Chemistry Chemical Physics* **2002**, 4, 812; c)J. Chen, S. Han, H. Zhao, J. Bai, L. Wang, G. Sun, Z. Zhang, X. Pan, J. Zhou, E. Xie, *Chemical Engineering Journal* **2017**, 320, 34.
[25] J. G. Choi, L. T. Thompson, *Applied Surface Science* **1996**, 93, 143.
[26] Z. Cao, H. Liu, L. Jiang, *Materials Horizons* **2020**, 7, 912.
[27] A. F. Visentin, M. J. Panzer, *ACS Appl Mater Interfaces* **2012**, 4, 2836.
[28] J. Serra Moreno, G. Maresca, S. Panero, B. Scrosati, G. B. Appetecchi, *Electrochemistry Communications* **2014**, 43, 1.
[29] M. Matsumoto, S. Shimizu, R. Sotoike, M. Watanabe, Y. Iwasa, Y. Itoh, T. Aida, *J Am Chem Soc* **2017**, 139, 16072.
[30] M. P. Mousavi, B. E. Wilson, S. Kashefolgheta, E. L. Anderson, S. He, P. Buhlmann, A. Stein, *ACS Appl Mater Interfaces* **2016**, 8, 3396.
[31] , https://doi.org/10.1787/9789264070349.

[32] a)L. Chen, T. Qiang, X. Chen, W. Ren, H. J. Zhang, *ACS Applied Polymer Materials* **2021**, 4, 357; b)S. Feng, S. Cao, Z. Tian, H. Zhu, D. Kong, *ACS Appl Mater Interfaces* **2019**, 11, 45844; c)E. S. Hosseini, S. Dervin, P. Ganguly, R. Dahiya, *ACS Appl Bio Mater* **2021**, 4, 163; d)W. Niu, Y. Zhu, R. Wang, Z. Lu, X. Liu, J. Sun, *ACS Appl Mater Interfaces* **2020**, 12, 30805.
[33] C. G. Vanginkel, C. A. Stroo, *Ecotox Environ Safe* **1992**, 24, 319.
[34] a)R. Thangavel, K. Kaliyappan, K. Kang, X. Sun, Y.-S. Lee, *Advanced Energy Materials* **2016**, 6; b)S. Zheng, J. Ma, Z.-S. Wu, F. Zhou, Y.-B. He, F. Kang, H.-M. Cheng, X. Bao, *Energy & Environmental Science* **2018**, 11, 2001.
[35] a)R. Alcantara, M. Jaraba, P. Lavela, J. L. Tirado, *Chem Mater* **2002**, 14, 2847; b)S. Hariharan, K. Saravanan, P. Balaya, *Electrochemistry Communications* **2013**, 31, 5; c)Q. Sun, Q.-Q. Ren, H. Li, Z.-W. Fu, *Electrochemistry Communications* **2011**, 13, 1462.
[36] S. Zheng, C. Zhang, F. Zhou, Y. Dong, X. Shi, V. Nicolosi, Z.-S. Wu, X. Bao, *Journal of Materials Chemistry A* **2019**, 7, 9478.
[37] a)J. Chang, M. Jin, F. Yao, T. H. Kim, V. T. Le, H. Yue, F. Gunes, B. Li, A. Ghosh, S. Xie, Y. H. Lee, *Advanced Functional Materials* **2013**, 23, 5074; b)X. Xiao, T. Ding, L. Yuan, Y. Shen, Q. Zhong, X. Zhang, Y. Cao, B. Hu, T. Zhai, L. Gong, J. Chen, Y. Tong, J. Zhou, Z. L. Wang, *Advanced Energy Materials* **2012**, 2, 1328.
[38] L. Migliorini, C. Piazzoni, K. Pohako-Esko, M. Di Girolamo, A. Vitaloni, F. Borghi, T. Santaniello, A. Aabloo, P. Milani, *Advanced Functional Materials* **2021**, 31.
[39] a)J. Halim, S. Kota, M. R. Lukatskaya, M. Naguib, M.-Q. Zhao, E. J. Moon, J. Pitock, J. Nanda, S. J. May, Y. Gogotsi, M. W. Barsoum, *Advanced Functional Materials* **2016**, 26, 3118; b)W. Feng, R. Wang, Y. Zhou, L. Ding, X. Gao, B. Zhou, P. Hu, Y. Chen, *Advanced Functional Materials* **2019**, 29.
[40] R. B. Rakhi, N. A. Alhebshi, D. H. Anjum, H. N. Alshareef, *J. Mater. Chem. A* **2014**, 2, 16190.
[41] a)C. Guo, C. Li, D. L. Kaplan, *Biomacromolecules* **2020**, 21, 1678; b)S. Zhao, C. Guo, A. Kumarasena, F. G. Omenetto, D. L. Kaplan, *ACS Biomater Sci Eng* **2019**, 5, 4808.
[42] K. V. Rajagopalan, *Annu Rev Nutr* **1988**, 8, 401.
[43] S. H. Zeisel, K. A. da Costa, *Nutr Rev* **2009**, 67, 615.
[44] U.S. Food and Drug Administration Department of Health and Human Services, **1984**, Title 21, https://www.accessdata.fda.gov/scripts/cdrh/cfdocs/cfcfr/cfrsearch.cfm?fr=184.1061.
[45] C. Boehler, S. Carli, L. Fadiga, T. Stieglitz, M. Asplund, *Nat Protoc* **2020**, 15, 3557.
[46] J. T. Reeder, Z. Q. Xie, Q. S. Yang, M. H. Seo, Y. Yan, Y. J. Deng, K. R. Jinkins, S. R. Krishnan, C. Liu, S. McKay, E. Patnaude, A. Johnson, Z. C. Zhao, M. J. Kim, Y. M. Xu, I. Huang, R. Avila, C. Felicelli, E. Ray, X. Guo, W. Z. Ray, Y. G. Huang, M. R. MacEwan, J. A. Rogers, *Science* **2022**, 377, 109.
[47] R. T. Tran, P. Thevenot, D. Gyawali, J. C. Chiao, L. Tang, J. Yang, *Soft Matter* **2010**, 6, 2449.